Computational Mechanics
https://doi.org/10.1007/s00466-025-02694-2

ORIGINAL PAPER

Quantifying the systematic and the random error for linear elastic particle-reinforced composites and reducing the variance by fixing the volume fraction

Shreyas Karthik Ravichandran[1] · **Binh Huy Nguyen**[1] · **Matti Schneider**[1,2,3]

Received: 29 April 2025 / Accepted: 9 September 2025
© The Author(s) 2025

Abstract
Two different sources of error emerge when computing the effective properties of materials with random microstructure: the random error which quantifies the fluctuations of the apparent properties computed on volume elements of finite size and the systematic error which is caused by the finite size of the considered volume element. Whereas the random error is apparent in computations, the systematic error is more subtle and requires much more effort to determine. How quickly these two errors decay for increasing volume-element size strongly depends on the way the volume element is selected - whereas the systematic error decays much faster than the random error for *periodized* ensembles, the opposite is true for *snapshot* ensembles in three spatial dimensions. Snapshot ensembles select the volume element as a part of a larger microstructure and correspond to the "real-world scenario" where a test specimen is cut from a larger material sample. Therefore, quantifying both the random and the systematic error for industrial composites is interesting and helpful for engineering applications. The work at hand studies the systematic and the random error for generated microstructures endowed with linear elastic constituents, both for periodized and non-periodized microstructures. We utilize computational micromechanics methods based on the fast Fourier transform (FFT) and evaluate the effective Young's modulus for composites with a plastic matrix and spherical as well as cylindrical reinforcements at industrial volume fractions. Moreover, we study the influence of the volume fraction on both the random and systematic errors, which leads to an unbiased variance-reduction strategy.

Keywords Stochastic homogenization · Random error · Systematic error · Random microstructure · Representative volume element · Variance reduction

1 Introduction

1.1 State of the art

Since its inception by Hill [1], the representative volume element (RVE) serves as the workhorse in computational mechanics of multiscale materials [2] with random microstructure [3–5]. Based on the observation that the randomness of such materials becomes smaller on larger and larger scales, the RVE is considered to be large enough to be representative for the microstructure and its inherent statistics [6].

The modern view on such multiscale materials was shaped, on the one hand, by mathematical works [7, 8] which provided the theoretical underpinnings of random materials, and, on the other hand, by working definitions for the practical engineer, e.g., the ideas provided by Drugan-Willis [9] or the statistical approach of Kanit et al. [10] based on the concept of the integral range [11, 12]. In fact, since around the 1990 s, developments in RVE methods were strongly driven by computational methods which require a much more quantitative definition of the RVE [13, 14].

✉ Matti Schneider
matti.schneider@uni-due.de

[1] Institute of Engineering Mathematics, University of Duisburg-Essen, Duisburg, Germany

[2] Center for Nanointegration Duisburg-Essen (CENIDE), Duisburg, Germany

[3] Fraunhofer Institute for Industrial Mathematics ITWM, Kaiserslautern, Germany

Published online: 06 October 2025

In a similar direction, there were more or less parallel developments on the heterogeneous multiscale method (HMM) [15–17] in the mathematics community and Finite Element Squared schemes (FE^2) [18–20] in computational mechanics. When trying to prove statements on the convergence behavior of the HMM and its predecessor [21], the presence of a so-called resonance error [22, 23] was noticed which precluded proving optimal convergence rates in this setting. The resonance error, originally emerging for periodic homogenization and unit cells which do not resolve the *natural* periodic unit cell, turned out to be present for random materials, as well. In the periodic setting, several methods for mitigating the resonance error were introduced [21, 24]. In the stochastic context, such endeavors turned out to be more subtle. We refer to the literature [25–30] for details. All of these mitigation techniques were worked out for thermal conductivity only.

The resonance error is closely connected to the error precluding a considered cell to be representative. Found independently in the engineering [10] and the mathematics community [31], the error under consideration may be naturally decomposed into two contributions: the random error, also called dispersion, quantifies the fluctuations of the apparent properties on unit cells of a fixed size, and the systematic error, or bias, which measures the difference of the mean apparent properties on cells of fixed size compared to the effective properties. By definition, the systematic error is a deterministic quantity, whereas the random error is stochastic in nature, i.e., may be reduced by a Monte Carlo strategy.

Classically, the systematic error was considered to be negligibly small [10], and the working definition on the RVE size involved the convergence behavior of the random error only, see Forest-Jeulin [32] for a modern account and some historical perspective. In particular, for a variety of materials, the convergence behavior of the random error is well documented, see Jeulin [33] and the reference therein. In the "standard case", the random error converges with the scaling of the central limit theorem (CLT), but both faster and slower convergence rates are possible for "pathological microstructures" [34–36].

The systematic error is more subtle. Only for simple ensembles [37–39], an explicit analysis of the convergence rate of the systematic error is possible. In the ideal scenario, the systematic error converges as the inverse of the volume, i.e., with twice the rate as the CLT. For particle-matrix composites, the situation turns out to be somewhat interesting. Traditionally, microstructure generators [40] use periodic boundary conditions to produce microstructures which avoid boundary effects. In contrast, real-world samples, e.g., obtained by X-ray computed microtomography [41, 42] record snapshots of the real material, leading to boundary effects, e.g., cut particles. It was observed that treating the latter ensembles leads to an inferior convergence rate of the systematic error compared to the optimal case, corresponding to the resonance error in HMM. For certain models pertinent to mathematical analysis, the emergence of this inferior convergence rate could be proved [43]. In contrast, the periodization strategy inherent to microstructure generators could be shown to provide the "optimal" convergence rate of the systematic error, both by computational investigations [44, 45] and by mathematical analysis.

1.2 Contributions

The work at hand may be considered a continuation of previous work [34] in thermal conductivity. Back then, the goal was to investigate the behavior of the systematic and the random error for *realistic microstructures*, requiring state of the art tools both for the microstructure generation [5] and computational resolution [46].

More precisely, matrix-inclusion composites were considered both with spherical and with cylindrical fillers at industrial volume fractions and with realistic material parameters. Such a scenario is most interesting for the engineering community and requires significant transfer work compared to purely academic studies typically performed to validate mathematical convergence proofs.

FFT-based computational homogenization methods [46–48] were put to use, which are based on a voxel description of the microstructure. Such methods permit to treat large-scale three-dimensional microstructures of industrial complexity, and the sharp convergence behavior under grid refinement was recently uncovered [49, 50] exploiting the superconvergence phenomenon [51] in homogenization, providing a theoretical basis for the findings. It was observed that the random error did not converge with the expected CLT rate, and the convergence behavior of the systematic error remained mysterious. It was argued that the systematic error was too small to enable scrutiny, whereas the unexpected decay behavior of the random error was attributed to long-range correlations visible in the local volume fractions and characteristic for industrial filler fractions.

The work at hand revisits these scenarios with the experience gained in the last couple of years. More precisely, the goal was to tackle the case of linear elasticity which is of primary interest to computational mechanics. In fact, although set in the framework of computational mechanics, the work at hand should be regarded as an *experimental study*, much like experimental mathematics may be used to find mathematical relationships. Actually, although convergence-rate estimates were provided for simple ensembles of microstructures materials, the actual magnitudes of the errors, i.e., the exact constant in the bound, are required for

engineering design! So, this is the primary question driving this manuscript:

What is the magnitude of both the systematic and the random error for industrial materials?

Specifically, we target linear elastic composites here, investigating whether the findings of Schneider et al. [34] transfer to this case. Moreover, we would like to assess the validity of traditional strategies to select the RVE size, e.g., the approach of Kanit et al. [10] which monitors the random error only. Such an approach was undertaken by Altendorf et al. [52] for short-fiber systems. As a bonus, we also investigate the influence of the volume fraction which turned out to be particularly significant for the previous work [34]. Typically, digital images obtained by X-ray computed tomography produce a scalar intensity field. To get hands on a segmented image, a suitable threshold needs to be selected. Apparently, the realized volume fraction depends strongly on the employed threshold, and in case the expected volume fraction is known by other means, e.g., from weighing the sample, this piece of information may be exploited. For the study at hand, we mimic this procedure by suitably scaling the level-set function of the particles, see Sect. 3.2.

A previously announced, the work at hand should be considered as an experimental procedure. As such, specific choices of the "measuring equipment" need to be highlighted, in particular compared to the previous study in thermal conductivity [34] The transfer from conductivity to the mechanical setting is substantial, as more equations need to be solved, the RVEs are larger and the considered material contrasts are larger, as well. To cope with these challenges, we devise a specific strategy to judge the current number of realizations to be sufficient based on an analysis of the confidence interval, see Sect. 3.4. These ideas, although straightforward in principle, provide a significant edge over previous attempts with a fixed number of realizations [34, 44, 45]. Of course, we also employ more computing power. Still, particularly interesting is the influence of the volume fraction on the obtained results.

This work is structured as follows: We provide a self-contained discussion of the systematic and the random error as well as their expected convergence behavior in Sect. 2, discuss the methods in Sect. 3 and report the computational results in Sect. 4. We discuss the ramifications in the conclusions Sect. 5.

2 The effective elastic properties of random materials and the associated errors

We consider a stationary and ergodic ensemble $\langle\cdot\rangle$ of stiffness tensors on the space $\mathbb{R}^d$ whose realizations are uniformly bounded from above and from below, i.e., there are positive constants $\alpha_\pm$, s.t. the inequalities

$$\alpha_- \|\boldsymbol{\varepsilon}\|^2 \leq \boldsymbol{\varepsilon} : \mathbb{C}(\boldsymbol{x}) : \boldsymbol{\varepsilon} \leq \alpha_+ \|\boldsymbol{\varepsilon}\|^2 \tag{2.1}$$

hold for all strains $\boldsymbol{\varepsilon} \in \mathrm{Sym}(d)$, almost every point $\boldsymbol{x} \in \mathbb{R}^d$ and almost every realization

$$\mathbb{C} : \mathbb{R}^d \to L(\mathrm{Sym}(d)). \tag{2.2}$$

For every macroscopic strain $\bar{\varepsilon} \in \mathrm{Sym}(d)$, we denote by $\boldsymbol{u}_{\bar{\varepsilon}}$ the displacement-corrector field associated to the specific realization $\mathbb{C}$, i.e., the vector field $\boldsymbol{u}_{\bar{\varepsilon}} \in H^1_0(\mathbb{R}^d)^d$, where $H^1_0(\mathbb{R}^d)^d$ denotes the closure of smooth vector fields with compact support w.r.t. the first-order Sobolev norm, which solves the corrector equation

$$\mathrm{div}\ \mathbb{C} : (\bar{\varepsilon} + \nabla^s \boldsymbol{u}_{\bar{\varepsilon}}) = \boldsymbol{0}, \tag{2.3}$$

where the symbol ∇^s stands for the symmetrized gradient. Although the corrector field $\boldsymbol{u}_{\bar{\varepsilon}}$ is not stationary, it may be shown [7, 8] that the associated strain

$$\boldsymbol{\varepsilon}_{\bar{\varepsilon}} \equiv \bar{\varepsilon} + \nabla^s \boldsymbol{u}_{\bar{\varepsilon}} \tag{2.4}$$

and stress fields

$$\boldsymbol{\sigma}_{\bar{\varepsilon}} \equiv \mathbb{C} : (\bar{\varepsilon} + \nabla^s \boldsymbol{u}_{\bar{\varepsilon}}) \tag{2.5}$$

are, in fact, stationary. The effective stress

$$\bar{\boldsymbol{\sigma}}_{\bar{\varepsilon}} = \langle \boldsymbol{\sigma}_{\bar{\varepsilon}} \rangle \tag{2.6}$$

is then defined via ensemble averaging the local stress field (2.5). By varying the prescribed strain $\bar{\varepsilon}$, the effective stiffness tensor $\mathbb{C}^{\mathrm{eff}} \in L(\mathrm{Sym}(d))$ is defined implicitly through the relation

$$\mathbb{C}^{\mathrm{eff}} : \bar{\varepsilon} = \bar{\boldsymbol{\sigma}}_{\bar{\varepsilon}}. \tag{2.7}$$

By elementary arguments, it may be shown that the effective stiffness $\mathbb{C}^{\mathrm{eff}}$ inherits the symmetry property and the validity of the bounds (2.1) from the local field $\mathbb{C}$.

To extract the effective stiffness of the just described model of random elastic materials, it is necessary to work with fields defined on bounded domains. For this reason, we consider additional ensembles $\langle\cdot\rangle_L$ whose realizations

$\mathbb{C}_L$ we also equip with the subscript L. More precisely, we consider cubic unit cells

$$Q_L = [0, L]^d \tag{2.8}$$

with edge length L, and we assume that almost all the realizations $\mathbb{C}_L$ are, in fact, Q_L-periodic. Because of the latter property, the effective stiffness $\mathbb{C}_L^{\text{eff}}$ may be computed by working on the periodic volume Q_L (2.8) only, to be detailed below.

Up to this point, the approximating realizations $\mathbb{C}_L$ and the original realizations $\mathbb{C}$ are not connected. To give an idea, we consider two classical scenarios [34]:

1. *Snapshot ensembles* arise from restricting realizations $\mathbb{C}$ of the full-space ensemble $\langle\cdot\rangle$ to the cell Q_L and extending the restricted field periodically to the full space.
2. *Periodized ensembles* [40, 43] periodize the law, i.e., have the same "construction principle" as the full-space ensemble, but take periodic boundary conditions into account.

The snapshot strategy is straightforward and is always applicable. It is also "natural" whenever digital images of real, i.e., non-digital, materials are considered, e.g., based on X-ray computed tomography.

The periodization strategy is more subtle, i.e., it requires the "construction principle" to be known. For instance, Poisson-Laguerre tessellations or certain matrix-inclusion composites fall into this category, see Jeulin [33] for an authorative overview. In fact, whenever a microstructure generator serves as the basis, only the approximating realizations $\mathbb{C}_L$ are available, and the effective stiffness (2.7) may only be obtained through the limiting procedure of increasing cell size.

To probe the effective stiffness (2.7) via the approximating ensemble $\mathbb{C}_L$ with periodic cell Q_L, we construct the apparent stiffness $\mathbb{C}_L^{\text{app}}$ similar to the effective stiffness (2.7), more precisely using the implicit relationship

$$\mathbb{C}_L^{\text{app}} : \bar{\boldsymbol{\varepsilon}} = \fint_{Q_L} \mathbb{C}_L : (\bar{\boldsymbol{\varepsilon}} + \nabla^s \boldsymbol{u}_{L,\bar{\boldsymbol{\varepsilon}}})\, d\boldsymbol{x}, \tag{2.9}$$

where the periodic field $\boldsymbol{u}_{L,\bar{\boldsymbol{\varepsilon}}} \in H^1_{\#}(Q_L)^d$ solves the cell problem

$$\operatorname{div} \mathbb{C} : (\bar{\boldsymbol{\varepsilon}} + \nabla^s \boldsymbol{u}_{L,\bar{\boldsymbol{\varepsilon}}}) = \boldsymbol{0} \tag{2.10}$$

and the dashed integral refers to the integral divided by the volume of the cube Q_L. In contrast to the deterministic effective stiffness (2.7), the apparent stiffness $\mathbb{C}_L^{\text{app}}$ is a random variable. Still, under suitable hypotheses on the connection between the ensembles $\langle\cdot\rangle_L$ and $\langle\cdot\rangle$, the apparent properties converge to the effective properties

$$\lim_{L\to\infty} \mathbb{C}_L^{\text{app}} = \mathbb{C}^{\text{eff}} \tag{2.11}$$

almost surely. Traditionally, a realization $\mathbb{C}_L$ is called representative volume element (RVE) if its apparent stiffness is sufficiently close to the effective stiffness (2.7), where the margin of tolerated error strongly depends on the application.

In practice, the definition of the RVE faces the challenge that the effective stiffness $\mathbb{C}^{\text{eff}}$ is not known. Traditionally, investigating the RVE size thus requires computing apparent properties on varying cell sizes (2.8) and quantifying the resulting differences. A more refined strategy was introduced by Kanit et al. [10], which is based on a natural decomposition of the discrepancy $\mathbb{C}^{\text{eff}} - \mathbb{C}_L^{\text{app}}$ into a deterministic and a random contribution

$$\mathbb{C}^{\text{eff}} - \mathbb{C}_L^{\text{app}} = \mathbb{C}^{\text{eff}} - \langle \mathbb{C}_L^{\text{app}} \rangle + \langle \mathbb{C}_L^{\text{app}} \rangle - \mathbb{C}_L^{\text{app}}, \tag{2.12}$$

which, by the binomial formula and taking the expectation, leads to the error decomposition [10, 31]

$$\left\langle \|\mathbb{C}^{\text{eff}} - \mathbb{C}_L^{\text{app}}\|^2 \right\rangle = \|\mathbb{C}^{\text{eff}} - \langle \mathbb{C}_L^{\text{app}} \rangle\|^2 + \left\langle \|\langle \mathbb{C}_L^{\text{app}} \rangle - \mathbb{C}_L^{\text{app}}\|^2 \right\rangle. \tag{2.13}$$

The first error $\left\|\mathbb{C}^{\text{eff}} - \langle \mathbb{C}_L^{\text{app}} \rangle\right\|$, called bias [10] or systematic error [31], is deterministic and measures the inability of the finite cell Q_L to capture the long-range correlations of the original ensemble. The second contribution, called dispersion [10] or random error [31], quantifies the fluctuations of the apparent stiffness $\mathbb{C}_L^{\text{app}}$ computed on the cell Q_L of fixed size.

The relative magnitudes of these errors determines which strategies for extracting the effective properties is actually effective. In case the systematic error is rather small, computing the empirical mean of the apparent stiffnesses for a number N of independent realizations $\mathbb{C}_{L,i}$

$$\hat{\mathbb{C}}_{L,N}^{\text{app}} = \frac{1}{N} \sum_{i=1}^{N} \mathbb{C}_{L,i}^{\text{app}} \tag{2.14}$$

turns out to be a clever strategy. Indeed, computing N apparent stiffnesses on a reasonably small cell does not require extraordinary computing facilities. In contrast, suppose that the random error is smaller than the systematic error. Then, computing multiple apparent stiffnesses on a specific cell size is not advised. Rather, working on increasing cell sizes Q_L is mandatory to obtain an accurate estimate for the

effective stiffness. Thus, it appears to be advisable to study the material under consideration.

Interestingly, this is not the end of the story. In fact, it was observed empirically that the systematic and the random error show different convergence rates in terms of the cell-edge length L, in general. More precisely, the random error typically shows the scaling

$$\sqrt{\left\langle \left\| \langle \mathbb{C}_L^{\mathrm{app}} \rangle - \mathbb{C}_L^{\mathrm{app}} \right\|^2 \right\rangle} \lesssim L^{-\frac{d}{2}} \tag{2.15}$$

familiar from the central limit theorem (CLT) for identically and independently distributed random variables. Indeed, the error scales as the inverse square root of the volume $\mathrm{vol}(Q_L) = L^d$ of the unit cell under consideration. The scaling (2.15) is only expected on suitably large scales and under sufficient de-correlation. For materials with long-range correlations, an inferior convergence rate may be expected, e.g., for infinitely long fibers [35]. A similar behavior was also observed for spherical inclusions [34] at high volume fractions.

The decay behavior of the systematic error is more subtle. For periodized ensembles, a convergence rate

$$\left\| \mathbb{C}^{\mathrm{eff}} - \langle \mathbb{C}_L^{\mathrm{app}} \rangle \right\| \lesssim L^{-d} \tag{2.16}$$

is expected from the investigation of certain analytically tractable models of coefficients [37–39]. However, previous investigations of matrix-inclusion composites and thermal conductivity [34] could not confirm this scaling, possibly due to the relative smallness of the systematic error compared to the random error. Snapshot ensembles, in contrast, often show the inferior decay rate

$$\left\| \mathbb{C}^{\mathrm{eff}} - \langle \mathbb{C}_L^{\mathrm{app}} \rangle \right\| \lesssim L^{-1} \tag{2.17}$$

independent of the dimension d, see Clozeau et al. [43] for an analytical result. Such a behavior is actually well-documented in the literature [21, 25, 26].

Depending on the relative scaling behavior, the two errors must be treated accordingly. For instance, in case of the favorable scaling (2.16), the systematic error will eventually become smaller than the random error. In this case, the strategy (2.14), or improvements thereof, should be favored.

In contrast, the scaling (2.17) is characteristic for snapshot ensembles, together with the CLT scaling (2.15) for the random error lead to the phenomenon that the magnitude of the systematic error will typically be much larger than the random error for sufficiently large volumes. Such a limiting argument motivated a number of works [25–30] which investigated strategies to reduce the systematic error or even improve its convergence rate for snapshot ensembles.

The work at hand is devoted to provide a quantification of the magnitude of the involved errors for two classes of industrial composites. Indeed, the scaling behavior of the errors alone may be secondary in view of suitably large or small constants involved in the estimates.

3 Methods

3.1 Generating periodic and snapshot microstructures

To assess the effect of taking snapshots of real microstructures and the influence of the volume fraction, we resort to microstructure-generation algorithms [5]. In this way, we are able to access the ground truth, i.e., the constructed example, leading to a reasonably fair comparison. The downside of this approach is, however, that generated microstructures represent a model of the actual microstructure, and may necessarily come with some simplifications compared to real microstructures. Moreover, the observed results – and, thus, the conclusions drawn – may depend on the microstructure model, and, possibly, the algorithm, chosen.

For the article at hand, we consider two kinds of matrix-inclusion composites whose generation algorithms are well-known and described here for the convenience of the reader. For a start, we investigate spherical fillers of identical size. There is quite a number of algorithms available for packing spheres to high volume fraction, e.g., the Lubachevsky-Stillinger algorithm [53], the Torquato-Jiao method [54], the force-biased packing scheme [55] or modifications of the Random Sequential Addtion method [56]. In this work, we consider the mechanical contraction method (MCM), introduced by Williams-Philipse [57] and embed into an optimization framework [58] later, which is our algorithm of choice due to its direct extension to packing spherocylinders.

The input of the MCM is the desired volume fraction ϕ, the sphere radius r and the number of spheres N. Moreover, a number of steps K and associated volume fractions $\phi_1, \phi_2, \ldots, \phi_K$ need to be specified, s.t. the volume fractions are increasing

$$0 < \phi_1 < \phi_2 < \ldots < \phi_K \tag{3.1}$$

and the final volume fraction ϕ_K coincides with the target volume fraction ϕ. For practical reasons, we also introduce a minimum distance $\delta > 0$ between the spheres as an algorithmic parameter to be specified.

For an initial edge-length L_0, which is assumed to be sufficiently large, the centers $\{\boldsymbol{x}_i^1\}_{i=1}^N$ are sampled randomly in the cube $[0, L_0]^3$. The mechanical-contraction method alternates between two phases: contraction and

overlap removal. Suppose the $(k-1)$-th step is completed for $k = 1, 2, \ldots, K$. For the subsequent step k, the cell-edge length L_k is chosen such that the targeted volume fraction ϕ_k is reached

$$\frac{N\,\frac{4}{3}\,\pi r^3}{L_k^3} \overset{!}{=} \phi_k, \quad \text{i.e.,} \quad L_k = \sqrt[3]{\frac{4}{3}\frac{N}{\phi_k}\,\pi}\, r. \tag{3.2}$$

Then, the previously obtained sphere centers $\{\boldsymbol{x}_i^{k-1}\}_{i=1}^N$ are rescaled

$$\boldsymbol{x}_i^k = \frac{L_k}{L_{k-1}}\,\boldsymbol{x}_i^{k-1}, \quad i = 1, 2, \ldots, K, \tag{3.3}$$

concluding the contraction phase. This procedure (3.3) may introduce overlap between the spheres. To remove this overlap, we introduce the quantity

$$\delta_{ij} = \langle 2r + \delta - \mathrm{dist}_k(\boldsymbol{x}_i, \boldsymbol{x}_j)\rangle_+, \quad 1 \le i < j \le N, \tag{3.4}$$

where the Macauley bracket is defined by

$$\langle\cdot\rangle_+ : \mathbb{R} \to \mathbb{R}, \quad z \mapsto \max(0, z), \tag{3.5}$$

and dist_k refers to the periodic distance between two points on the cell $[0, L_k]^3$. The quantity δ_{ij} vanishes precisely if the inner term

$$2r + \delta - \mathrm{dist}_k(\boldsymbol{x}_i, \boldsymbol{x}_j) \le 0 \tag{3.6}$$

is non-positive, i.e., the inequality

$$\mathrm{dist}_k(\boldsymbol{x}_i, \boldsymbol{x}_j) \ge 2r + \delta \tag{3.7}$$

is satisfied. Put differently, as the parameter δ is positive, the two sphere centers $\boldsymbol{x}_i$ and $\boldsymbol{x}_j$ are more than twice the radius apart, i.e., the associated spheres with radius r do not overlap. Moreover, the parameter δ ensures an additional minimum distance between the spheres.

To ensure that the inequality (3.7) holds, the MCM considers the objective function

$$F(\boldsymbol{x}_1, \boldsymbol{x}_2, \ldots, \boldsymbol{x}_N) = \frac{1}{2} \sum_{1 \le i < j \le N} \delta_{ij}^2, \tag{3.8}$$

where the square is introduced to make the function F differentiable. As the function F arises as a sum of squares, the function F vanishes if and only if all the quantities δ_{ij}, defined in eq. (3.4), vanish. Moreover, the value zero emerges as the minimum value of the objective function (3.8). In particular, although the function (3.8) is not convex, it is straightforward to identify a minimizer with objective value 0 as a *global minimizer*.

With the goal of minimizing the objective function (3.8) in mind, we take a look at the gradient

$$\nabla_{\boldsymbol{x}_i} F(\boldsymbol{x}_1, \boldsymbol{x}_2, \ldots, \boldsymbol{x}_N) = -\sum_{j=1,\, j\neq i}^{N} \delta_{ij}\,\frac{\boldsymbol{\xi}_{ij}}{\|\boldsymbol{\xi}_{ij}\|}, \tag{3.9}$$

where $\boldsymbol{\xi}_{ij}$ is the vector connecting the centers $\boldsymbol{x}_i$ and $\boldsymbol{x}_j$, i.e., the vector realizing the minimum distance $\mathrm{dist}_k(\boldsymbol{x}_i, \boldsymbol{x}_j)$. To minimize the objective, a gradient update

$$\boldsymbol{x}_i^{a+1} = \boldsymbol{x}_i^a - h\,\nabla_{\boldsymbol{x}_i} F(\boldsymbol{x}_1^a, \boldsymbol{x}_2^a, \ldots, \boldsymbol{x}_N^a) \tag{3.10}$$

is used, where a stands for the iteration index, and a step size $h = 1/2$ is used. More explicitly, the iterative procedure

$$\boldsymbol{x}_i^{a+1} = \boldsymbol{x}_i^a + \frac{1}{2}\sum_{j=1,\, j\neq i}^{N} \delta_{ij,a}\,\frac{\boldsymbol{\xi}_{ij}^a}{\|\boldsymbol{\xi}_{ij}^a\|} \tag{3.11}$$

is considered. To understand the formula (3.11), it is helpful to consider only two spheres centered at $\boldsymbol{x}_i$ and $\boldsymbol{x}_j$ with positive overlap $\delta_{ij,a}$. The prescription (3.11) pushes the centers $\boldsymbol{x}_i$ and $\boldsymbol{x}_j$ apart along the direction $\boldsymbol{\xi}_{ij}^a$ of shortest connection, and the distance is chosen such that both centers move precisely by an amount of $\delta_{ij,a}/2$. Put differently, if no other overlaps were present, the current overlap would be directly removed by a single iteration (3.11).

The MCM method works quickly and robustly. For the article at hand, we choose a target volume fraction ϕ of 30%, the radius $r = 25\mu$m and a minimum distance $\delta = 10\mu$m. Moreover, the contraction proceeds by 10% steps, i.e., $\phi_k = k \cdot 10\%$. Examples of generated unit cells are shown in Fig. 1 for $2^3 = 8$, $4^3 = 64$ and $8^3 = 512$ inclusions. For the work at hand, thousands of such microstructures had to be generated. On a standard laptop, generating the largest of the shown cells with 512 inclusions takes slightly over one second. Obtaining the representation on a regular mesh with 128^3 voxels takes about 0.1s.

With the same protocol, also the rather large volume elements may be obtained, which are intended to serve as the ground truth for a representative volume element. An example of such a microstructure is shown in Fig. 2a, containing $64^3 = 262\,144$ spheres, and voxelized by 1024^3 voxels. The MCM method takes around 7min on a standard laptop, and most of the time is spent on setting up the cell-linked lists [59] which speed up the mutual distance calculations required in Eq. (3.4) significantly. The subsequent voxelation takes less than one minute.

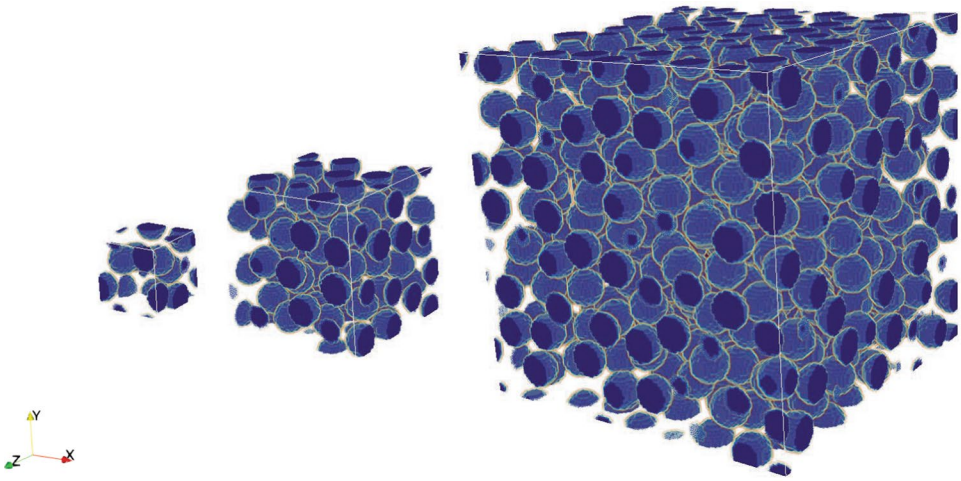

(a) 32^3 (b) 64^3 (c) 128^3

Fig. 1 Illustrating the size of the periodic cells with spherical inclusions, distinguishing the number of voxels

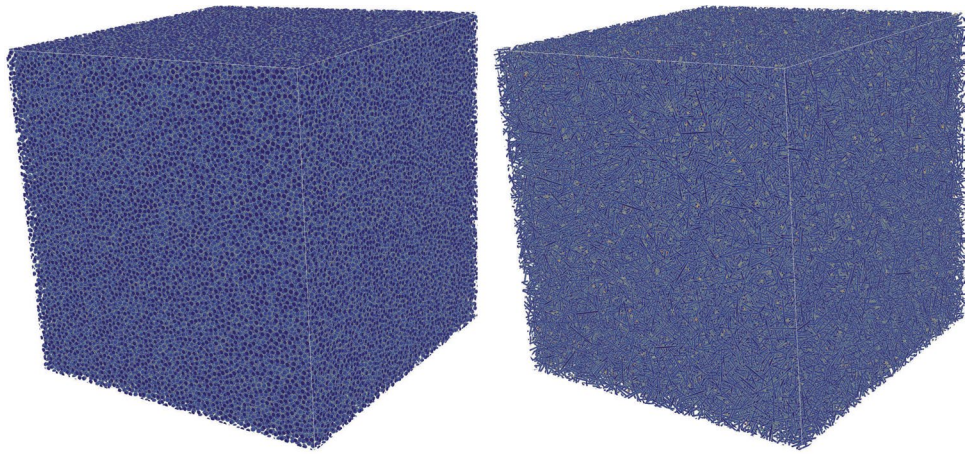

(a) Spherical fillers (b) Fibers

Fig. 2 Realizations of reference cells

The second class of microstructures we consider are fiber composites. More precisely, we restrict to straight cylindrical fibers with uniform length ℓ and diameter d. In addition to the fiber-volume fraction ϕ, the fiber-orientation tensor of fourth order $\mathbb{A}^\star$ is prescribed. For N fibers with (unit) direction vectors $\{\boldsymbol{p}_i\}_{i=1}^N$, the empirical fiber-orientation tensor of fourth order [60–62] is defined via

$$\mathbb{A}_N = \frac{1}{N}\sum_{i=1}^{N} \boldsymbol{p}_i \otimes \boldsymbol{p}_i \otimes \boldsymbol{p}_i \otimes \boldsymbol{p}_i. \tag{3.12}$$

Although higher-order fiber-orientation tensors may be considered, it is empirically well-established that the fourth-order fiber-orientation tensor is suitable for prescribing the elastic properties of the fiber composite, at least in case the fibers show little curvature [63–65]. The space of realizable fiber-orientation tensors is known explicitly [66]. For the work at hand, we prescribe an isotropic fiber-orientation tensor, i.e., we expect the mechanical behavior of the fiber composite to be isotropic, as well.

For generating fiber composites, we use the sequential addition and migration (SAM) algorithm [58]. Similar to the MCM, the SAM alternates between two phases, a volume-fraction increasing and an overlap-removing stage. However, in contrast to the MCM, the cell $[0, L]^3$ remains fixed throughout the algorithm. Rather, the number N_k of fibers is increased to match the desired volume fraction ϕ_k

$$\frac{N_k \pi \ell d^2}{4\, L^3} \overset{!}{=} \phi_k, \quad \text{i.e.,} \quad N_k = \left\lceil \frac{4\phi_k L^3}{\pi \ell d^2} \right\rfloor, \tag{3.13}$$

where the rectangular bracket selects the closest integer for a given real input. We set $N_0 = 0$ for consistency reasons. Moreover, to reduce the error in volume fraction, the fiber length ℓ is also slightly adjusted via

$$\ell_N = \frac{4\phi L^3}{\pi d^2 \left[\frac{4\phi L^3}{\pi \ell d^2}\right]}. \tag{3.14}$$

In fact, the contraction approach [57] may also be used for cylindrical fibers. However, the SAM approach comes with a number of advantages. For a start, considering fewer particles in for the beginning stages speeds up the algorithm. Secondly, in case the volume increments are too small, the MCM approach fails to produce high volume fractions [57], in particular industrial ones. The reason is that other fibers block the way of specific fibers when trying to reach higher volume fractions. To proceed, it would be required to cross the other fiber, in turn making a sufficiently large contraction step necessary.

The first phase of SAM samples fibers, i.e., for $k = 1, 2, \ldots, K$, we draw $N_k - N_{k-1}$ fiber centers $\boldsymbol{x}_i$ and fiber directions $\boldsymbol{p}_i$ for $i = N_{k-1} + 1, N_{k-1} + 2, \ldots, N_k$. The fiber centers are sampled from the uniform distribution on the cube $[0, L]^3$, whereas the directions are drawn from the uniform distribution on the unit sphere S^2 in the three-dimensional Euclidean space. In this sampling phase, the previously placed fibers remain unaltered from the previous step.

The second phase of the SAM targets an overlap removal via the objective function

$$\begin{aligned} &F(\boldsymbol{x}_1, \ldots, \boldsymbol{x}_N, \boldsymbol{p}_1, \boldsymbol{p}_2, \ldots, \boldsymbol{p}_N) \\ =&\frac{1}{2} \sum_{1 \le i < j \le N} \delta_{ij}^2 + \frac{N}{4} \left\| \boldsymbol{A}^\star - \boldsymbol{A}_N \right\|^2, \end{aligned} \tag{3.15}$$

where we suppress the dependence on the index k for notational clarity and the factors δ_{ij} are defined via

$$\delta_{ij} = \langle D + \delta - \|\boldsymbol{k}_{ij}\| \rangle_+. \tag{3.16}$$

Here, $\delta > 0$ is a minimum distance and the vector $\boldsymbol{k}_{ij}$ realizes the minimum distance

$$\operatorname{dist}\left(\boldsymbol{x}_i + \frac{s}{2}\boldsymbol{p}_i, \boldsymbol{x}_j + \frac{t}{2}\boldsymbol{p}_j\right) \to \min_{s,t \in [0,1]} \tag{3.17}$$

between the central line segments of the spherocylinders i and j. Actually, spherocylinders, i.e., cylinders with half-spheres attached, are considered to simplify the overlap check. For fibers which are long enough, attaching a cap appears to be not critical.

As for spheres, a vanishing of the factors δ_{ij} defined in eq. (3.16) ensure that the central line segments of the i-th and j-th spherocylinders are at least a distance $D + \delta$ apart, i.e., the corresponding spherocylinders do not overlap and a minimum distance of δ is maintained. Moreover, the objective function (3.15) vanishes if and only if all the factors (3.16) vanish and the fiber-orientation constraint

$$\mathbb{A}^\star \stackrel{!}{=} \mathbb{A}_N \tag{3.18}$$

is satisfied exactly.

Based on the optimization framework (3.15), the overlap-removal phase proceeds by a gradient-descent approach. Some care has to be taken when selecting a suitable step-size and performing the update step on the directions. Also, an efficient implementation should exploit suitable spatial data structures, e.g., nested Verlet lists [67]. We refer to Schneider [58] for details.

In this work, we consider cylindrical fibers with a diameter of 10μm and a length of 200μm, i.e., an aspect ratio of 20. The desired volume fraction is $\phi = 15\%$, obtained in 5% -steps, and the targeted orientation is isotropic. Moreover, a minimum distance of $\delta = 2\mu$m is enforced.

Examples of generated cells are shown in Fig. 3 with a voxel resolution of 1μm. The $(100\mu\text{m})^3$ cell comprises 76 fibers of length 201.0378μm, whereas 611 fibers of length 200.0507μm are contained in the $(200\mu\text{m})^3$ cell. The larger

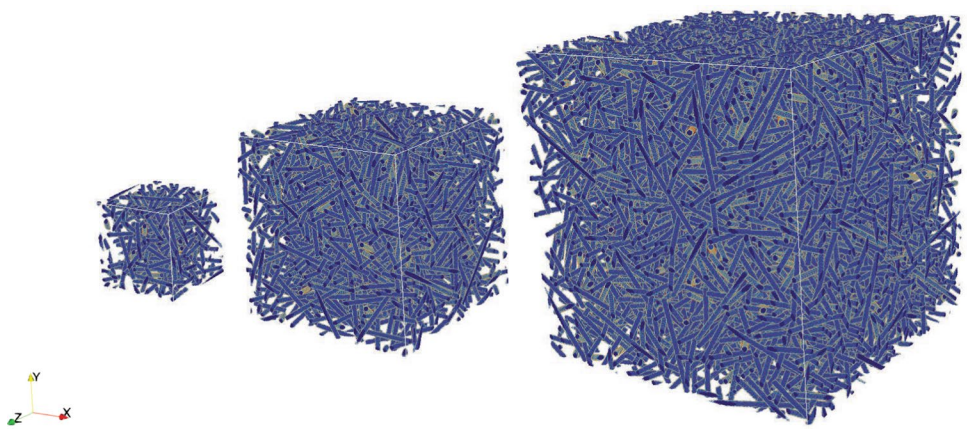

(a) 100^3 (b) 200^3 (c) 300^3

Fig. 3 Illustrating the size of the periodic cells with reinforcing fibers, parameterized by the number of voxels

cell with an edge-length $300\mu\mathrm{m}$ leads to 2 062 cylindrical inclusions with a length of $200.0629\mu\mathrm{m}$. Generating the latter cell requires less than 10s on a standard laptop, and the voxelation on a 300^3 grid takes slightly more than 1s.

The reference cell considered has a size of $[0, 1024\mu\mathrm{m}]^3$, and a sample with 82 027 fibers is shown in Fig. 2b. On a standard laptop, it takes slightly more than two minutes to generate such a cell and about one minute to voxelize the structure.

The constructed unit cells for both spherical and cylindrical fillers are periodic because the periodic distance on the cells is used. To generate snapshot examples, we create a periodic unit cell with doubled edge length and consider one eighth of the generated periodic cell.

3.2 Optimized volume fraction

Using the proper volume fraction is critical for obtaining an accurate estimate for the effective stiffness of a matrix-inclusion composite. Indeed, classical series expansions in the material contrast [68, §20] reveal that the volume fraction appears in the first order term. Put differently, any error in the volume fraction is likely to induce an error in the estimated stiffness. Therefore, it appears imperative to reduce these errors.

In the work at hand, there are two principal sources of errors in the volume fraction. For a start, although the volume fraction was prescribed exactly in the microstructure generation procedures described in Sect. 3.1 for periodic composites, the subsequent voxelation procedure leads to an error. Actually, different consistent voxelation paradigms may be chosen. We decide the membership of the voxel to the proper phase based on the centroid of the voxel. On average, such a procedure matches the desired volume fraction quite accurately, with an error that is proportional to the voxel edge-length. The second source of uncertainty of the volume fraction arises from the snapshot procedure. Although the volume fraction is matched – up to voxelation error – on the large scale, i.e., the periodic cell, considering only a cut volume leads to a dispersion of the volume fraction.

To mitigate these errors, we use a simple procedure which we explain for the case of spherical fillers first. For a target volume fraction ϕ and N particles with radius r, the realized volume fraction computes as

$$\frac{4\,N r^3}{3\,L^3} \tag{3.19}$$

in the cubic cell $[0, L]^3$. We wish to counterbalance the inaccuracies of the actual volume fraction by rescaling the radius slightly. We proceed as follows. We introduce a function

$$\Phi : \mathbb{R}_{>0} \to \mathbb{R}, \quad \Phi(\rho) = \frac{4\,N(\rho\, r)^3}{3\,L^3}, \tag{3.20}$$

i.e., we use a rescaling factor $\rho \approx 1$ to update the radius. More precisely, we follow the logic of Newton's method, i.e., we select the increment $\triangle\rho$ based on the approximation

$$\phi \overset{!}{=} \Phi(1 + \triangle\rho) \approx \Phi(1) + \Phi'(1)\,\triangle\rho. \tag{3.21}$$

By the homogeneous scaling behavior

$$\Phi(\rho) = \Phi(1)\,\rho^3, \tag{3.22}$$

one directly obtains the identity

$$\Phi(1) + \Phi'(1)\,\triangle\rho = \Phi(1) + 3\,\Phi(1)\,\triangle\rho. \tag{3.23}$$

With this insight, we may solve the equation (3.21) for the increment

$$\triangle\rho = \frac{\phi - \Phi(1)}{3\,\Phi(1)}. \tag{3.24}$$

Suppose that a proxy $\tilde{\phi}$ for the volume fraction associated to some radius r is given. Then, we may use the iterative procedure

$$\phi_k = \tilde{\phi}(r_k), \tag{3.25}$$

$$r_{k+1} = \left(1 + \frac{\phi - \phi_k}{3\,\phi_k}\right) r_k, \tag{3.26}$$

to obtain better and better estimates for the virtual radius r_∞ that permits to match the desired accuracy in the volume fraction.

For fiber composites, a similar procedure may be followed, rescaling both the fiber length and the diameter

$$(d, \ell) \mapsto (\rho\, d, \rho\, \ell) \tag{3.27}$$

by a positive factor $\rho \approx 1$. More precisely, the proxy $\tilde{\phi}$ for fibers depends on both the diameter and the fiber length, and we consider the algorithm

$$\phi_k = \tilde{\phi}(d_k, \ell_k), \tag{3.28}$$

$$\rho_k = \left(1 + \frac{\phi - \phi_k}{3\,\phi_k}\right) \tag{3.29}$$

$$d_{k+1} = \rho_k\, d_k, \tag{3.30}$$

$$\ell_{k+1} = \rho_k\, \ell_k. \tag{3.31}$$

Last but not least, let us emphasize that we use the described procedure in case of snapshot ensembles, as well. In this scenario, the volume-fraction errors turn out to be larger than in the periodized case.

3.3 FFT-based computational micromechanics

Suppose that a stiffness distribution $\mathbb{C}_L$ is given on the cubic cell $Q_L = [0, L]^3$. For two-phase composites, the class of microstructured materials of principal importance to this work, this stiffness distribution takes only two values: the stiffness tensor of the matrix and the corresponding tensor of the inclusion. For the realized stiffness $\mathbb{C}_L$, the apparent stiffness is defined by the implicit relationship (2.9)

$$\mathbb{C}_L^{\text{app}} : \bar{\boldsymbol{\varepsilon}} = \fint_{Q_L} \mathbb{C}_L : (\bar{\boldsymbol{\varepsilon}} + \nabla^s \boldsymbol{u}_{L,\bar{\boldsymbol{\varepsilon}}})\, d\boldsymbol{x}, \tag{3.32}$$

where the periodic field $\boldsymbol{u}_{L,\bar{\boldsymbol{\varepsilon}}} \in H^1_{\#}(Q_L)^d$ solves the cell problem (2.10)

$$\operatorname{div} \mathbb{C} : (\bar{\boldsymbol{\varepsilon}} + \nabla^s \boldsymbol{u}_{L,\bar{\boldsymbol{\varepsilon}}}) = \boldsymbol{0} \tag{3.33}$$

and the dashed integral refers to the integral divided by the volume of the cube Q_L.

To obtain an approximation of the apparent stiffness $\mathbb{C}_L^{\text{app}}$, the balance equation (3.33) needs to be discretized and solved. More precisely, the discretized form of the problem (3.33) reads

$$\operatorname{div}_{\text{h}} \mathbb{C}_h : (\bar{\boldsymbol{\varepsilon}} + \nabla_h^s \boldsymbol{u}_{L,\bar{\boldsymbol{\varepsilon}},h}) = \boldsymbol{0}, \tag{3.34}$$

where h stands for the mesh parameter, the operators ∇_h^s and $\operatorname{div}_{\text{h}}$ refer to discrete versions of the symmetrized gradient and the divergence operator and the stiffnesses $\mathbb{C}_h$ signify a discrete approximation to the stiffness field $\mathbb{C}$. Different kinds of discretizations are possible: Spectral methods [47, 48, 69], finite differences [70–72] and finite elements [73–75] are the most popular in the homogenization context. FFT-based computational micromechanics [47, 48] regards the problem (3.34) as a linear system

$$\boldsymbol{A}_h \boldsymbol{u}_{L,\bar{\boldsymbol{\varepsilon}},h} = \boldsymbol{b}_h \tag{3.35}$$

with

$$\begin{aligned} \boldsymbol{A}_h \boldsymbol{u}_{L,\bar{\boldsymbol{\varepsilon}},h} &\equiv \operatorname{div}_{\text{h}} \mathbb{C}_h : \nabla_h^s \boldsymbol{u}_{L,\bar{\boldsymbol{\varepsilon}},h} \quad \text{as well as} \\ \boldsymbol{b}_h &\equiv -\operatorname{div}_{\text{h}} \mathbb{C}_h : \bar{\boldsymbol{\varepsilon}}, \end{aligned} \tag{3.36}$$

and uses the constant-coefficient preconditioner

$$\boldsymbol{P}_h \boldsymbol{v}_h \equiv \operatorname{div}_{\text{h}} \mathbb{C}^0 : \nabla_h^s \boldsymbol{v}_h \tag{3.37}$$

involving a homogeneous reference stiffness $\mathbb{C}^0$. Originally, the Richardson-type method [76]

$$\boldsymbol{u}_{L,\bar{\boldsymbol{\varepsilon}},h}^{k+1} = \boldsymbol{u}_{L,\bar{\boldsymbol{\varepsilon}},h}^{k} - \boldsymbol{P}_h^{-1} \left(\boldsymbol{A}_h \boldsymbol{u}_{L,\bar{\boldsymbol{\varepsilon}},h}^{k} - \boldsymbol{b}_h \right), \quad k = 0, 1, 2, \ldots, \tag{3.38}$$

termed *basic scheme*, was used. Nowadays, the conjugate-gradient method [77, 78] with the preconditioner (3.37) is preferred. There are also other solvers with reduced memory consumption, see the dedicated review articles [46, 79, 80] for details. To complete the discussion here, two issues need to be clarified:

1. What properties are expected from the iterative scheme (3.38) and CG preconditioned by the operator (3.37)?
2. How is the (pseuso-)inverse of the preconditioner (3.37) obtained?

For the first item: Under the assumptions (2.1), the basic scheme (3.38) requires on the order of κ iterations for desired accuracy and a suitably chosen reference material [81]. Here,

$$\kappa = \frac{\alpha_+}{\alpha_-} \tag{3.39}$$

stands for the *elastic material contrast*. In particular, the iteration count of the iterative scheme (3.38) is bounded independently of the mesh spacing h. For the conjugate-gradient method with the constant-coefficient preconditioner (3.37), the classic bounds on the iteration count for CG show that the iteration count is bounded by the square root $\sqrt{\kappa}$ of the elastic material contrast (3.39), again independent of the grid spacing.

The preconditioning strategy just described hinges on the ability to evaluate the inverse of the operator (3.37) efficiently and to high accuracy, see item 2. For FFT-based micromechanics, it was observed that such an inversion is possible for *any discretization on a regular grid* and periodic boundary conditions by utilizing the discrete Fourier transform. Indeed, any constant-coefficient finite-difference operator transforms into a Fourier multiplier via the Fourier transform. Then, the inverse of the reference problem (3.37) is directly obtained by inverting the symbol of the operator (3.37) and reverting to real space by an inverse Fourier transform. The literature on FFT methods contains a variety of explicit formulas for such inversion procedures and different discretizations, see the review articles [46, 79, 80] for an overview and a discussion of the respective advantages and disadvantages.

The discretization on a regular grid makes meshing complex microstructures simple. However, the local solution fields lack the accuracy of a boundary-conforming grid.

Still, the numerically computed apparent stiffness converges to the exact apparent stiffness for this specific realization with a rate that is linear in the voxel size [49, 50]. Thus, to reduce the resolution error by a factor of ten, the number of voxels per edge length should be amplified by a factor of ten, as well. For the accuracy required in engineering applications, such regular-grid representations of complex microstructures were shown to be very powerful.

For the work at hand, we use the staggered-grid discretization [71] and utilize the conjugate gradient method [77, 78], solved to a relative accuracy of 10^{-9}.

3.4 Determining the number of realizations

For the article at hand, we consider the Young's modulus

$$E = \frac{1}{\boldsymbol{e}_1 \otimes \boldsymbol{e}_1 : \mathbb{C}^{-1} : \boldsymbol{e}_1 \otimes \boldsymbol{e}_1} \tag{3.40}$$

as the quantity of interest. In particular, we investigate the apparent Young's modulus

$$E_L^{\mathrm{app}} = \frac{1}{\boldsymbol{e}_1 \otimes \boldsymbol{e}_1 : (\mathbb{C}_L^{\mathrm{app}})^{-1} : \boldsymbol{e}_1 \otimes \boldsymbol{e}_1} \tag{3.41}$$

on the cell $Q_L = [0, L]^3$ as an approximation for the effective Young's modulus

$$E^{\mathrm{eff}} = \frac{1}{\boldsymbol{e}_1 \otimes \boldsymbol{e}_1 : (\mathbb{C}^{\mathrm{eff}})^{-1} : \boldsymbol{e}_1 \otimes \boldsymbol{e}_1} \tag{3.42}$$

We consider N independent and identically distributed realizations $E_{L,i}^{\mathrm{app}}$ of the Young's modulus (2.9). We estimate the mean Young's modulus

$$\langle E_L^{\mathrm{app}} \rangle_L \tag{3.43}$$

by the empirical mean

$$\hat{E}_{L,N}^{\mathrm{app}} = \frac{1}{N} \sum_{i=1}^{N} E_{L,i}^{\mathrm{app}}. \tag{3.44}$$

To judge the accuracy of this estimate, we consider the associated unbiased sample variance

$$\hat{s}_{L,N}^2 = \frac{1}{N-1} \sum_{i=1}^{N} \left(E_{L,i}^{\mathrm{app}} - \hat{E}_{L,N}^{\mathrm{app}} \right)^2. \tag{3.45}$$

To obtain a confidence level $1 - \alpha$, the associated confidence interval has the form

$$\left[\hat{E}_{L,N}^{\mathrm{app}} - \hat{e}_{L,N}, \hat{E}_{L,N}^{\mathrm{app}} + \hat{e}_{L,N} \right] \tag{3.46}$$

with the error

$$\hat{e}_{L,N} = t_{(1-\alpha/2),N-1} \frac{\hat{s}_{L,N}}{\sqrt{N}} \tag{3.47}$$

that involves the quantile $t_{(1-\alpha/2),N-1}$ of student's t-distribution with $N - 1$ degrees of freedom. For instance, for $\alpha = 1\%$ and $N = 10$, this quantile reads

$$t_{0.995,9} \approx 3.25 \tag{3.48}$$

to two significant digits. For a large number of samples, student's t-distribution is approximately equal to the normal distribution, and we may take

$$t_{0.995,N} \approx 2.58 \tag{3.49}$$

to two significant digits for the confidence level $\alpha = 1\%$.

To assess the systematic error, we monitor the quantity

$$\epsilon_{\mathrm{sys}} = \frac{\left| \hat{E}_{L,N}^{\mathrm{app}} - E^{\mathrm{ref}} \right|}{E^{\mathrm{ref}}} \tag{3.50}$$

with a reference modulus E^{ref} computed on a rather large cell $Q_{L^\star}$, where the edge length $L^\star$ exceeds the monitored cell-size L sufficiently. We report on the dimensionless errors

$$\frac{\hat{e}_{L,N}}{E^{\mathrm{ref}}} \tag{3.51}$$

and

$$\frac{\hat{e}_{L^\star,N^\star}}{E^{\mathrm{ref}}}, \tag{3.52}$$

where $N^\star$ refers to the number of samples considered for the large cell $Q_{L^\star}$. In practice, we monitored the errors (3.51) and (3.52) to provide a criterion whether the number of samples N and $N^\star$ is sufficient.

In addition to the systematic error (3.50), we also report on the random error via the quantity

$$\epsilon_{\mathrm{ran}} = \frac{\hat{s}_{L,N}}{E^{\mathrm{ref}}} \tag{3.53}$$

which may be considered as a coefficient of variation. By using the same rescaling in eq.s (3.50) and (3.53), it is possible to compare the magnitude of the estimated systematic and the random error.

4 Computational investigations

4.1 Setup

We investigate elastic composites with E-Glass fillers and elastic parameters

$$E = 72\text{GPa} \quad \text{and} \quad \nu = 0.22 \tag{4.1}$$

inside a polyamide 66 matrix with moduli

$$E = 3\text{GPa} \quad \text{and} \quad \nu = 0.4, \tag{4.2}$$

following Hessman et al. [82]. The simulations were carried out on a computing workstation with two AMD EPYC 9354 32 core processors, 1.12 TB of RAM and Ubuntu 22.04.4.

The software for generating microstructures as described in Sect. 3.1 follows the description in Schneider [58] and Mehta-Schneider [83]. The voxelization is based on on a voxel-center strategy, i.e., each voxel is assigned to the phase of its center. For computing the apparent elastic properties of the realized microstructured elastic materials, we rely on an in-house FFT-based computational micromechanics code [84, 85] and use the discretization on a staggered grid [71], together with the conjugate-gradient method [77, 78].

The snapshot ensembles were created by considering on eighth of a suitably selected periodic microstructure. For selecting the number N of realizations considered, we monitor the width of the associated confidence interval, see eq. (3.51) and eq. (3.52).

4.2 Spherical inclusions

We consider microstructures with spherical fillers generated by the MCM algorithm as detailed in Sect. 3.1.

More precisely, we consider monodisperse spheres with a radius 25μm at a volume fraction of 30% with a minimum distance of 10μm between the inclusions. The resulting microstructures were resolved by voxels with an edge length of 3.76246μm which is roughly twice as fine as in the related study [34] on thermal conductivity.

We consider microstructures images of sizes 32^3, 64^3 and 128^3. For reference, we rely on 1024^3 voxel images.

The obtained results are summarized in Table 1 and plotted in Fig. 4.

We observe the following. For snapshot ensembles without optimized volume fractions, i.e., the ones considered closest to what is available in experiments, the systematic and the random errors are on the same level, i.e., the systematic error is about 25% higher than the random error. Moreover, both turn out to be rather high. For the smallest element size, $L = 32h$, the systematic error reaches almost 10%. For the $L = 128h$-cells, the systematic error exceeds 2%. The convergence rate of both errors scales as $1/L$, compare the blue curve in Fig.s 4a and b.

For periodized emsembles without optimized volume fractions, we observe that the systematic error is smaller than the random error consistently. Even for the smallest cell with 8 inclusions, the systematic error (about 1%) is smaller than for the largest cell with 512 spheres and snapshot ensembles (about 2%). In terms of scaling, we notice that the systematic error shows an L^{-3}-decay, see the red curve in Fig. 4a, conforming to the expectation (2.16). The random error, see Fig. 4b shows the CLT scaling (2.15).

Table 1 Statistics of the computed Young's modulus in GPa for spheres and periodic (PER) as well as snapshot (CUT) ensembles with optimized volume fraction (OVF) enabled (+) or disabled (-)

	OVF	Len	# Sim	Mean	Std	Sys. error	Rand. error	CI error
		L/h	N	$\hat{E}^{\text{app}}_{L,N}$ (3.44)	$\hat{s}_{L,N}$ (3.45)	ϵ_{sys} (3.50)	ϵ_{ran} (3.53)	$\hat{e}_{L,N}$ (3.47)
PER	−	32	3000	5.997739	0.1206104	1.043010%	2.010931%	0.0953401%
	−	64	3000	5.926046	0.0406712	0.164778%	0.686313%	0.0321498%
	−	128	1000	5.937889	0.0154268	0.034727%	0.259803%	0.0211216%
CUT	−	32	3000	6.477959	0.4757026	9.133208%	7.343403%	0.3760337%
	−	64	3000	6.204032	0.2049057	4.518398%	3.302783%	0.1619740%
	−	128	1000	6.071143	0.1038940	2.279635%	1.711275%	0.1422467%
PER	+	32	3000	5.997728	0.1204052	1.042838%	2.007514%	0.0951780%
	+	64	3000	5.926023	0.0405708	0.165171%	0.684622%	0.0320705%
	+	128	3000	5.937223	0.0154859	0.023518%	0.260827%	0.0122413%
	+	1024	10	5.935827	0.0006716	–	0.011314%	0.0116286%
CUT	+	32	3000	6.465528	0.2340355	8.923785%	3.619744%	0.1850006%
	+	64	3000	6.205166	0.0728148	4.537509%	1.173455%	0.0575587%
	+	128	1000	6.072259	0.0254523	2.298437%	0.419158%	0.0348481%

The underscored line serves as the reference for calculating the relative error

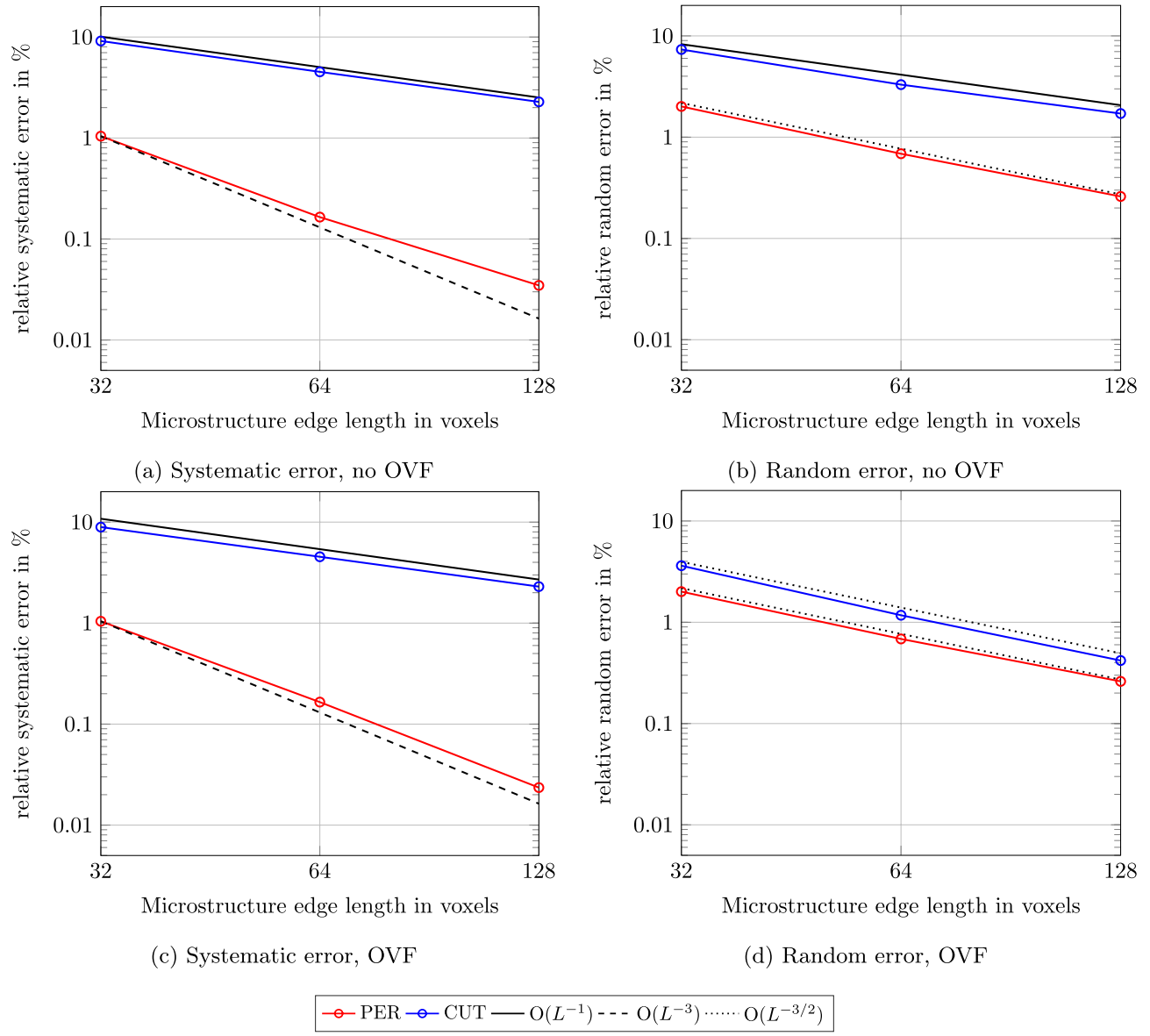

Fig. 4 Systematic and random error for periodic (PER) and snapshot (CUT) ensembles with spherical fillers without (top) and with (bottom) optimized volume fraction (OVF)

So, in contrast to the related study [34] in thermal conductivity, the optimal scaling of the systematic error could be observed, presumably due to the higher level of the systematic error.

We turn our attention to snapshot ensembles with optimized volume fraction. These microstructures represent a model of experimentally obtained digital images where the segmentation procedure accounts for the expected volume fraction which might be known by alternative measurements, e.g., weighing. The most striking difference concerns the random error: it is reduced by roughly a factor of two, at least. Also, the convergence rate of the random error is improved, see Fig. 4d, to the expected CLT scaling instead of the $1/L$-scaling prominent for the snapshot ensembles without optimized volume fraction, see Fig. 4b. In fact, this inferior convergence rate was also observed in thermal conductivity [34]. The authors argued that this convergence behavior is caused by the volume fractions alone based on a weak contrast expansion. The results obtained here may be considered as an experimental verification of their analysis.

Concerning the systematic error, the volume-fraction correction preserves the mean apparent properties up to four significant digits. In particular, the rescaling procedure does not infer a bias and may be considered *safe* in this regard.

Similar to the work [34], we investigate the empirical accuracy properties of the considered strategies for the ensemble at hand.

More precisely, we consider the following question: What is the probability of obtaining a result which is δ-close to the obtained effective properties estimates with high fidelity before. More precisely, we study the two accuracy levels $\delta = 1\%$ as well as $\delta = 0.1\%$, and count the realizations which are δ-close. The results are contained in Table 2. For periodized ensembles, roughly 50% of the realizations of the cells with 8 spheres are 1%-close to the effective properties, regardless of whether the volume fractions are optimized or not. The next larger cell with 64 inclusions comes with a more than 99.9% probability that this kind of accuracy is reached, at least in the periodic setting. For the snapshot ensembles, even the cells with 512 spherical inclusions only have a 2% probability to be 1%-close, at least if volume-fraction optimization is turned off. Interestingly, activating the optimized volume fraction decreases the probability to reach 1% fidelity. At first glance, this result appears counterintuitive, as we saw in Table 1 that the systematic error remains unaffected, whereas the random error is significantly reduced in this case. However, the truth of the story is that the systematic error is simply too large. To elaborate, let us consider the case with 128^3 voxels, i.e., 512 spherical inclusions. The systematic error exceeds 2% slightly. If optimized volume fraction is turned on, the random error, encoded by the relative standard deviation (3.53), lies at roughly 0.4%. Assuming a normal distribution, the 0.9999 quantile is about 3.7190 times the standard deviation over the mean. As this quotient exceeds five for the current example, such a scenario almost never happens. In contrast, turning optimized volume fractions on increases the normalized standard deviation to roughly 1.7%. Thus the coefficient of variation is about 4/3, and there is a non-zero probability of (accidentally) hitting the desired confidence level.

To sum up, optimizing volume fraction does its job - it reduces the variance for stochastic homogenization. However, this strategy does not alter the systematic error. Should the latter be too large, considering a single shot only does not lead to an improvement over the naive snapshot strategy. Optimized volume fractions are useful if and only if multiple realizations of the same cell size are investigated, and a Monte-Carlo strategy is used to estimate the mean apparent properties. For this setup, higher fidelity may be reached with the same number of samples, or, equivalently, the same level of fidelity is reached by fewer samples.

Table 2 Empirical probability (in %) of being 1%-close (left) and 0.1%-close(right) to the reference value for spherical inclusions

OVF	Len	PER	CUT	PER	CUT
-	32	50.09	0.15	4.04	0.01
-	64	99.98	0.23	25.53	0.01
-	128	100.00	1.96	69.14	0.02
+	32	50.05	0.00	4.02	0.00
+	64	99.98	0.00	25.57	0.00
+	128	100.00	0.00	70.78	0.00

Last but not least, we investigate the confidence level $\delta = 0.1\%$, see Table 2. For the snapshot ensembles, such an accuracy is out of (practical) reach. For periodized ensembles, the largest cell size leads to a 70% probability of being that accurate with a single run. These observations confirm the superiority of the periodization strategy [43, 86] in the case of spherical fillers.

4.3 Fiber composites

We turn our attention to cylindrical reinforcements. We generated fiber microstructures based on the SAM algorithm [58, 83], where the fiber-length distribution is concentrated at 200μm and each fiber has a diameter of 10μm. Filled to a volume fraction of 15% in 5% steps, a minimum distance of 4μm was enforced between the fibers, and an isotropic fiber-orientation state described by the fourth-order fiber-orientation tensor (3.12) was targeted. The resulting microstructures were discretized by a voxel length of $h = 2\mu$m, and we considered the cases $L = 100\,h$, $L = 200\,h$ and $L = 300\,h$ as our regular cases to be investigated, considering the large cells $L = 1000\,h$ as our reference.

The results of the simulations are collected in Table 3.

We make the following observations.

For snapshot ensembles without optimized volume fractions, the systematic error exceeds the random error consistently, in contrast to thermal conductivity [34]. For instance, the smallest cell has a systematic error of about 3% and a random error of about 2.4%. This error level is rather high, but considering the larger cells lead to reasonable engineering accuracy. Concerning the decay of the errors, see Fig. 5a and Fig. 5b, the convergence rates are $1/L$ for the systematic error and $L^{-3/2}$ for the random error. Thus, the expected resonance (2.17) and CLT scalings (2.15) are observed. As the random error decays faster than the systematic error, the empirical strategy of Kanit et al. [10] for selecting the RVE size appears to be unsafe in this scenario. Indeed, Kanit et al. [10] proposed to fit the decay of the random error to determine the RVE size. However, such a strategy is only recommended in case the systematic error is comparatively small. For linear elastic fiber composites as considered in the work at hand, this assumption is not satisfied: the systematic error exceeds the random error *and* decays faster. Therefore, it is recommended to augment the strategy [10] by a study on the systematic error.

Taking a look at the periodized fiber ensembles without optimized volume fractions, we observe that the systematic error is smaller than the random error except for the smallest cell. In fact, the smallest cell is a bit special as the fiber

Table 3 Statistics of the computed Young's modulus in GPa for fibers and periodic (PER) as well as snapshot (CUT) ensembles with optimized volume fraction (OVF) enabled (+) or disabled (-)

	OVF	Len	# Sim	Mean	Std	Sys. error	Rand. error	CI error
		L/h	N	$\hat{E}^{\mathrm{app}}_{L,N}$ (3.44)	$\hat{s}_{L,N}$ (3.45)	ϵ_{sys} (3.50)	ϵ_{ran} (3.53)	$\hat{e}_{L,N}$ (3.47)
PER	−	100	3000	5.085673	0.0136726	0.311263%	0.268845%	0.0126539%
	−	200	3000	5.071411	0.0050837	0.029936%	0.100242%	0.0047049%
	−	300	1000	5.070662	0.0028178	0.015177%	0.055571%	0.0045169%
CUT	−	100	1000	4.914972	0.1167534	3.055709%	2.375465%	0.1871561%
	−	200	1000	4.987624	0.0446106	1.622692%	0.894426%	0.0715109%
	−	300	1000	5.012805	0.0243267	1.126009%	0.485291%	0.0389958%
PER	+	100	10,000	5.085648	0.0135360	0.310766%	0.266160%	0.0068615%
	+	200	10,000	5.071434	0.0049840	0.030391%	0.098277%	0.0025265%
	+	300	3000	5.070573	0.0027582	0.013417%	0.054396%	0.0025527%
	+	1000	20	5.069893	0.0004192	–	0.008269%	0.0060093%
CUT	+	100	3000	4.912471	0.1079666	3.105039%	2.197806%	0.0999224%
	+	200	3000	4.988043	0.0409568	1.614426%	0.821101%	0.0379053%
	+	300	600	5.013261	0.0218776	1.117020%	0.436394%	0.0452750%

The underscored line serves as the reference for calculating the relative error

length coincides with the cell-edge length. For periodic boundary conditions, fibers may thus interact with themselves, possibly leading to a perturbed correlation for this cell size. All in all, the systematic error is still rather low at roughly 0.3%. Concerning the decay of the systematic error and the random error, see Fig. 5a and b, we observe that the systematic error shows the L^{-3}-decay expected from theory (2.16), whereas the CLT scaling (2.15) is observed for the random error. Compared to the snapshot ensembles, the errors, both systematic and random, are roughly an order of magnitude smaller for the periodized ensembles. Moreover, the systematic error converges with a faster rate. These observations confirm theoretical results [43] about the superiority of considering periodized microstructure-generation tools [10, 86] whenever possible to multiscale schemes in mechanics [2]. The smallest periodic cell with 100 voxels per edge leads to higher accuracy than the largest snapshot cell with 300 voxels per edge, although the latter has $3^3 = 27$ times the size!

The influence of the volume-fraction optimization is rather small for the fiber composites, see Fig. 5c and d. In fact, the random error is reduced slightly both for snapshot and periodized ensembles, whereas the systematic error appears unaffected (to three significant digits). Presumably, this smaller influence compared to the spherical fillers comes from two circumstances. For a start, the considered volumes are much larger. The smallest cell for fiber inclusions has 100^3 voxels, which is only slightly smaller than the largest cell considered for spherical fillers with 128^3 voxels. Moreover, the error made *per particle* is also smaller because the fibers are resolved by more voxels on average. To be more precise, the spheres are resolved by about 1228.8 voxels, on average, for the largest 1024^3 cell. In contrast, 1828.7 voxels resolve a single cylindrical fiber on average for the 1000^3 cell. Thus, roughly 50% more voxels are used for discretizing the fiber compared to the sphere case.

On the positive side, we also notice that the optimized volume fraction protocol does not induce a bias. We consider the empirical accuracy properties of the different strategies for the cylinderical fibers, as well. The results for being δ-close to the effective properties is shown in Table 4 for the two accuracy levels $\delta = 1\%$ and $\delta = 0.1\%$.

We observe that all realizations of the periodized ensemble are 1%-close to the representative Young's modulus. For the snapshot ensembles, even the largest considered cell with 300^3 voxels has only a probability of about 1/5 that 1% accuracy is reached with a single realization. Thus, considering multiple realizations is mandatory for this setup to reach representative values. However, as the largest considered cell size comes with a systematic error exceeding 1%, an accuracy below 1% appears to be unreachable with this setup, and even larger cells should be considered. Please notice that optimizing the volume fractions does not have a significant effect on the fiber composites, which we already saw for the systematic and the random errors. With little surprise, we notice that a similar conclusion may be drawn for the empirical accuracy properties.

The tighter confidence level $\delta = 0.1\%$ may be reached for periodized ensembles and a volume element with an edge length of about twice the fiber lengths with more than 97% probability. Thus, the current investigation fortifies current practice [58, 83] of using twice the fiber (mean) length as the RVE edge length, at least for the periodized setting. For snapshot ensembles, a fidelity of $\delta = 0.1\%$ is not realistic.

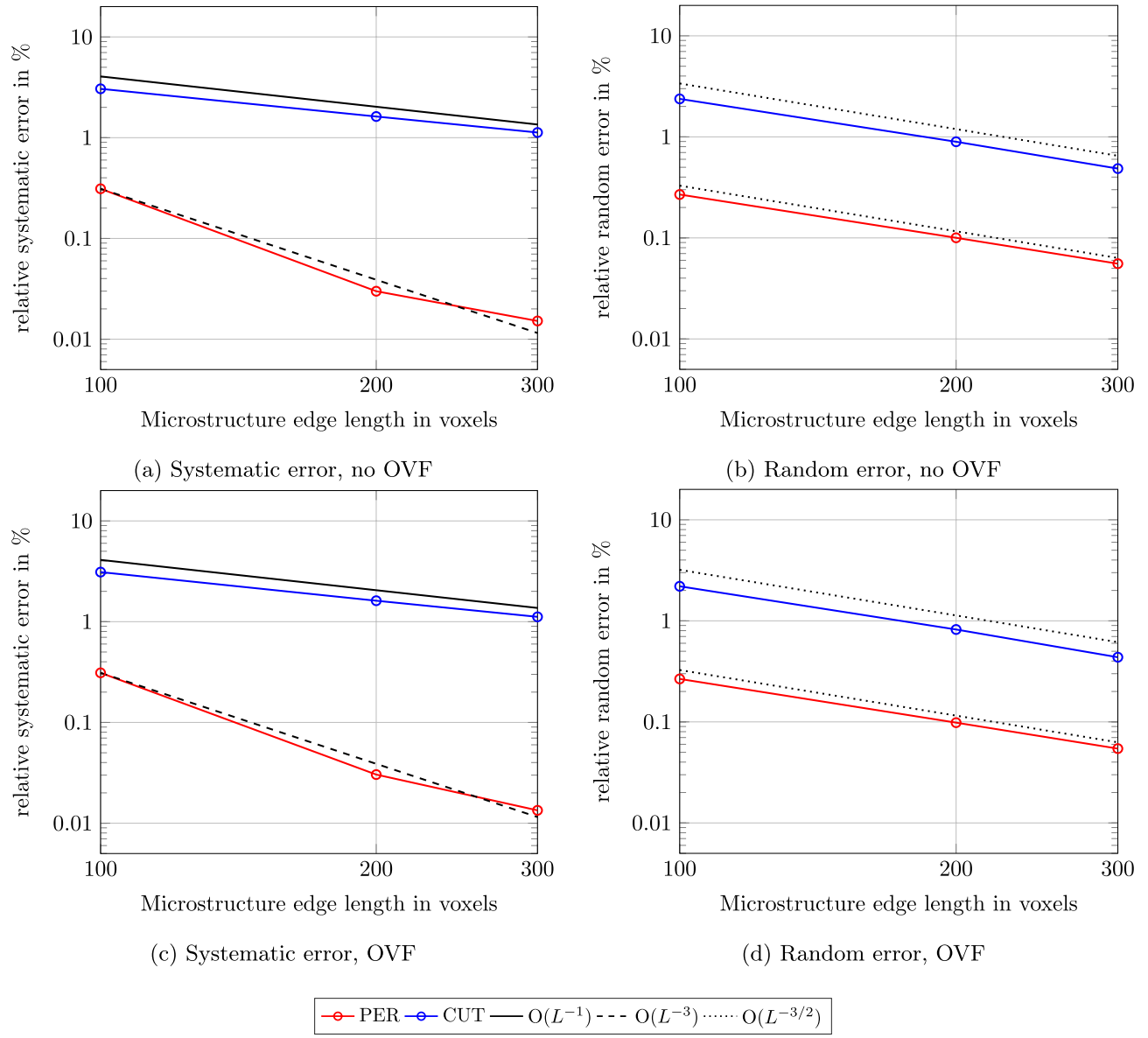

Fig. 5 Systematic and random error for periodic (PER) and snapshot (CUT) ensembles with fiber reinforced microstructures without (top) and with (bottom) optimized volume fraction (OVF)

Table 4 Empirical probability (in %) of being 1%-close (left) and 0.1%-close(right) to the reference value for fibers

OVF	Len	PER	CUT	PER	CUT
−	100	100.00	0.57	1.23	0.00
−	200	100.00	2.20	97.83	0.00
−	300	100.00	22.87	100.00	0.00
+	100	100.00	0.34	1.30	0.01
+	200	100.00	1.58	97.76	0.00
+	300	100.00	21.92	100.00	0.00

4.4 The influence of the material contrast

We investigate the influence of material contrast on the magnitude of bot the systematic and the random error in this section. Whereas the elastic constants of the e-glass fibers show little variation in applications, quite a number of different matrix materials are in use, like polyamide 6 (PA6), polyamide 6.6 (PA6.6), poplypropylene (PP) or polybutylene terephthalate (PBT). These thermoplastic matrices all show different elastic constants, and we wish to investigate the influence of these changes on the conclusions drawn previously.

In analogy to the spherical inclusions microstructures in Sect. 4.2, we choose to generate a periodized ensemble with optimized volume fractions of sizes 32^3, 64^3, 128^3 and the largest size 1024^3 for the reference. Three material contrasts are considered by halving and doubling the original Young's

Table 5 Statistics of the computed Young's modulus in GPa for spheres from periodic ensembles with different material contrasts

Contrast	Len	# Sim	Mean	Std	Sys. error	Rand. error	CI error
	L/h	N	$\hat{E}^{\mathrm{app}}_{L,N}$ (3.44)	$\hat{s}_{L,N}$ (3.45)	ϵ_{sys} (3.50)	ϵ_{ran} (3.53)	$\hat{e}_{L,N}$ (3.47)
12	32	10,000	10.997224	0.1693985	0.910495%	1.554400%	0.004636%
	64	10,000	10.885190	0.0579585	0.117525%	0.531827%	0.001586%
	128	5000	10.900250	0.0218219	0.020668%	0.200237%	0.000844%
	1024	19	10.897998	0.0008774	–	0.008051%	0.000437%
24	32	10,000	5.926646	0.1122996	1.024817%	1.914244%	0.010605%
	64	10,000	5.857652	0.0387647	0.151249%	0.660778%	0.003661%
	128	10,000	5.867801	0.0147304	0.021744%	0.251092%	0.001391%
	1024	19	5.866525	0.0005924	–	0.010098%	0.001019%
48	32	10,000	3.117316	0.0659980	1.055336%	2.139484%	0.022541%
	64	10,000	3.079380	0.0230387	0.174452%	0.746856%	0.007869%
	128	3000	3.085580	0.0087663	0.026562%	0.284180%	0.005466%
	1024	19	3.084761	0.0003551	–	0.011511%	0.002209%

The underscored line serves as the reference for calculating the relative error

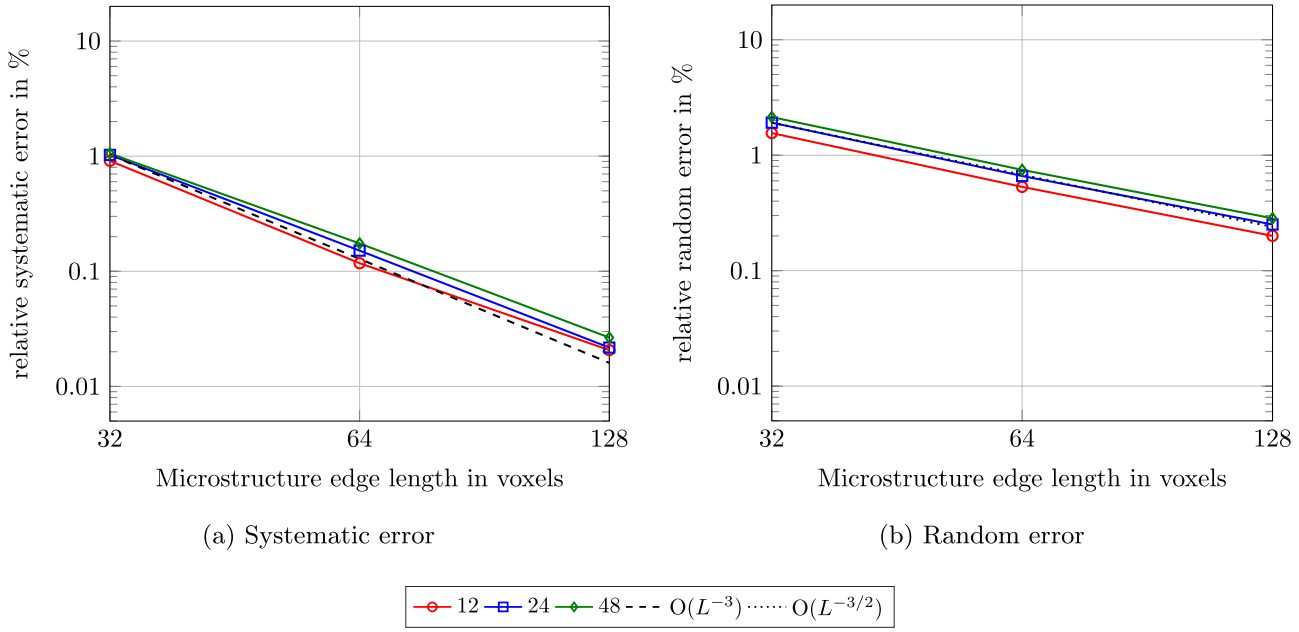

(a) Systematic error (b) Random error

Fig. 6 Systematic and random errors for periodized ensembles of spherical fillers with optimized volume fraction and different material contrasts

modulus of the polyamide 66 matrix to 6 GPa and 1.5 GPa, respectively. The statistics of the simulations are assembled in Table 5 and plotted in Fig. 6.

Please note that we use the composite voxel technique [87, 88] in the form detailed in the publication [89] for this study. Originally, we hoped that composite voxels lead to an increased accuracy. However, there were some issues not related to the manuscript at hand, and we decided to resort to plain voxels. For composite voxels, we observe that both systematic and random errors for the original material contrast are slightly smaller than those recorded in Table 1. For instance, for the smallest cell with eight inclusions, we observe the improvement of 1.7% and 4.6% in the systematic and the random error, respectively. Such improvement does not alter our observations on the asymptotic behavior of the errors. We turn our attention to the halving and doubling material contrasts. Both the systematic and the random errors behave rather similarly for all considered three contrasts, i.e., take values of about 1% and 2%, respectively, for the smallest cell size $L = 32h$. Whereas the three material contrasts preserve the accuracy up to two, three and four significant digits for lengths $L = 32h$, $L = 64h$ and $L = 128h$, respectively, the errors for the lowest material contrast of twelve are consistently smaller than that the other two, as higher contrasts are typically more challenging to address. Nevertheless, the systematic error is smaller than the random error regardless the material contrast. In terms of scaling, as observe in Fig. 6 that the convergence rates

Table 6 Empirical probability (in %) of being 1%-close (left) and 0.1%-close(right) to the reference value for spherical inclusions

Contrast	Len	$\delta = 1\%$	$\delta = 0.1\%$
12	32	50.86	5.53
	64	93.47	14.23
	128	100.00	38.89
24	32	43.90	4.62
	64	86.34	11.69
	128	99.99	30.47
48	32	40.50	4.47
	64	81.05	10.12
	128	99.93	27.71

of both errors are as expected for all three contrast cases. Interestingly, the scaling of the random errors in Fig. 6b are almost identical with respect to the contrasts.

Concerning the empirical probability at two accuracy levels $\delta = 1\%$ and $\delta = 0.1\%$, we present the results of three contrasts in Table 6. In agreement with the magnitudes of the systematic error in Table 2, for the same volume element size, the smaller contrast has higher probability of being δ -close to the its respective reference values. Specifically, the smallest unit cell has roughly 50% probability to be 1% -close to its reference result for a material contrast of twelve. This number drops to 43.9% and 40.5% for contrasts of 24 and 48, respectively. However, the lower probability is not linearly proportional to the increasing contrast.

To sum up this section, we observe that the relative magnitude between the systematic and random errors, as well as, their convergence rates are insensitive to the investigated material contrasts. Yet, as the absolute magnitude of the errors are increasing with higher contrast, albeit only logarithmically, and the corresponding empirical probability consequently declines.

5 Conclusions

We conclude the following:

1. For elastic composites with spherical and cylindrical fillers, we could show the expected convergence behavior of the systematic and the random error for both periodized and snapshot ensembles except for the random error for snapshot ensembles which showed a $1/L$-decay, in line with the arguments of Schneider et al. [34].
2. Concerning the magnitude of the individual error, we observed, for snapshot ensembles, that the systematic error exceeds the random error, and, in addition, converges slower. In particular, methods for reducing the systematic error gain importance - in contrast to conductivity [34] where the systematic errors could be neglected for engineering applications.
3. We showed in Sect. 4.4 that the results are not strongly dependent on the material contrast. Thus, for variations of the matrix material typical in industry, the drawn conclusions remain valid.
4. Our work sheds more light on the different strategies used in various situations for dealing with random materials. If microstructure generators are available, these should be used in such a way that periodized ensembles are generated. Then, single realizations provide good estimates for the RVE size [58, 83]. In contrast, for real-word digital-image data, our snapshot model predicts that multiple realizations are required to gain an estimate for the apparent properties of the unit cell under consideration, and multiple cell sizes need to be monitored to assess the RVE size [10].
5. Our findings question the validity of a previous report [90] which discredits the superiority of periodized ensembles and periodic boundary conditions.
6. We introduced a method to prescribe the exact volume fraction both for periodized and snapshot ensembles. Whereas the influence turned out to be miniscule for periodized ensembles – highlighting the advantages of regular grids once more – a strong influence could be discerned for snapshot ensembles and spherical inclusions: the magnitude of the random error was decreased and the decay behavior was improved, as well. As an additional benefit, prescribing the volume fraction did not have an impact on the systematic error. Put differently, prescribing the volume fractions via postprocessing leads to an unbiased variance-reduction strategy for random matrix-inclusion composites. We refer to the works [91, 92] for alternative variance-reduction approaches in stochastic homogenization.
7. We observed that the errors – both systematic and random – turned out to be significantly lower for cylindrical inclusions than for spherical inclusions, see also Altendorf et al. [52]. Of course, the considered volume elements were larger, but even for the comparable sizes, the errors for the fiber systems turned out to be smaller. Our take on this phenomenon is that for fibers, higher-order statistical data is prescribed in terms of the fiber-orientation tensor. In contrast, apart from the fixed volume fraction, the spherical inclusions enjoy more freedom. Moreover, the prescribed fiber-orientation tensor may lead to a restriction of the dispersion due to some long-range effects implicitly required by the orientation constraint.

Acknowledgements The authors acknowledge support from the European Research Council within the Horizon Europe program - project 101040238. We thank the anonymous reviewers for their constructive

comments and remarks.

Funding Open Access funding enabled and organized by Projekt DEAL.

Data availability The data that support the findings of this study are available from the corresponding author upon reasonable request.

Open Access This article is licensed under a Creative Commons Attribution 4.0 International License, which permits use, sharing, adaptation, distribution and reproduction in any medium or format, as long as you give appropriate credit to the original author(s) and the source, provide a link to the Creative Commons licence, and indicate if changes were made. The images or other third party material in this article are included in the article's Creative Commons licence, unless indicated otherwise in a credit line to the material. If material is not included in the article's Creative Commons licence and your intended use is not permitted by statutory regulation or exceeds the permitted use, you will need to obtain permission directly from the copyright holder. To view a copy of this licence, visit http://creativecommons.org/licenses/by/4.0/.

References

1. Hill R (1963) Elastic properties of reinforced solids: some theoretical principles. J Mech Phys Solids 11(5):357–372
2. Matouš K, Geers MGD, Kouznetsova VG, Gillman A (2017) A review of predictive nonlinear theories for multiscale modeling of heterogeneous materials. J Comput Phys 330:192–220
3. Ostoja-Starzewski M (2006) Material spatial randomness: from statistical to representative volume element. Probab Eng Mech 21(2):112–132
4. Gitman IM, Askes H, Sluys L (2007) Representative volume: existence and size determination. Eng Fract Mech 74(16):2518–2534
5. Bargmann S, Klusemann B, Markmann J, Schnabel JE, Schneider K, Soyarslan C, Wilmers J (2018) Generation of 3d representative volume elements for heterogeneous materials: a review. Prog Mater Sci 96:322–384
6. Beran MJ (1968) Statistical continuum theories. Wiley, Hoboken
7. Papanicolaou GC, Varadhan SRS (1981) Boundary value problems with rapidly oscillating random coefficients. In: Random fields, Vol. I, II (Esztergom, 1979), vol. 27 of *Colloq. Math. Soc. János Bolyai*, pp. 835–873, North-Holland, Amsterdam-New York
8. Kozlov SM (1979) Averaging differential operators with almost periodic, rapidly oscillating coefficients. Math USSR-Sbornik 35(4):481
9. Drugan WJ, Willis JR (1996) A micromechanics-based nonlocal constitutive equations and estimates of representative volume element size for elastic composites. J Mech Phys Solids 44:497–524
10. Kanit T, Forest S, Galliet I, Mounoury V, Jeulin D (2003) Determination of the size of the representative volume element for random composites: statistical and numerical approach. Int J Solids Struct 40(13–14):3647–3679
11. Matheron G (1989) Estimating and choosing. Springer, Berlin
12. Lantuéjoul C (2002) Geostatistical simulation—models and algorithms. Springer, Berlin
13. Moumen A, Kanit T, Imad A (2021) Numerical evaluation of the representative volume element for random composites. Eur J Mech A/Solids 86:104181
14. Gitman IM, Askes H, Sluys LJ (2007) Representative volume: existence and size determination. Eng Fract Mech 74(16):2518–2534
15. E W, Engquist B, (2003) The heterogeneous multi-scale methods. Commun Math Sci 1:87–133
16. Weinan E, Engquist B, Li X, Ren W, Vanden-Eijnden E (2007) Heterogeneous multiscale methods: a review. Comput Phys Commun 3:367–450
17. Abdulle A, Weinan E, Engquist B, VandenEijnden E (2012) The heterogeneous multiscale method. Acta Numer 21:1–87
18. Feyel F (1999) Multiscale fe2 elastoviscoplastic analysis of composite structures. Comput Mater Sci 16:344–354
19. Feyel F, Chaboche JL (2000) Fe2 multiscale approach for modelling the elastoviscoplastic behaviour of long fibre sic/ti composite materials. Comput Methods Appl Mech Eng 183(3–4):309–330
20. Miehe C (2002) Strain-driven homogenization of inelastic microstructures and composites based on an incremental variational formulation. Int J Numer Meth Eng 55:1285–1322
21. Hou TY, Wu X-H (1997) A multiscale finite element method for elliptic problems in composite materials and porous media. J Comput Phys 134:169–189
22. Weinan E, Ming P, Zhang P (2005) Analysis of the heterogeneous multiscale method for elliptic homogenization problems. J Am Math Soc 18(1):121–156
23. Abdulle A (2005) On a priori error analysis of fully discrete heterogeneous multiscale fem. Multiscale Model Simul 4:447–459
24. Blanc X, Bris C (2010) Improving on computation of homogenized coefficients in the periodic and quasi-periodic settings. Netw Heterogeneous Med 5(1):1–29
25. Gloria A (2011) Reduction of the resonance error - part 1: approximation of homogenized coefficients. Math Models Methods Appl Sci 21(8):1601–1630
26. Gloria A, Habibi Z (2016) Reduction in the resonance error in numerical homogenization ii: correctors and extrapolation. Found Comput Math 16:217–296
27. Arjmand D, Runborg O (2016) A time dependent approach for removing the cell boundary error in elliptic homogenization problems. J Comput Phys 341:206–227
28. Mourrat J (2019) Efficient methods for the estimation of homogenized coefficients. Found Comput Math 19:435–483
29. Abdulle A, Arjmand D, Paganoni E (2019) Exponential decay of the resonance error in numerical homogenization via parabolic and elliptic cell problems. CR Math 357(6):545–551
30. Bella P, Fischer J, Josien M, Raithel C (2024) Boundary layer estimates in stochastic homogenization 1–48. arXiv:2403.12911
31. Gloria A, Otto F (2011) An optimal variance estimate in stochastic homogenization of discrete elliptic equations. Ann Probab 39(3):779–856
32. Jeulin D, Forest, S (2024) Statistical approach to the representative volume element size of random composites. In: Digital Materials, ch. 2, 55–1111, John Wiley & Sons, Ltd
33. Jeulin D (2024) Morphological models of random structures, vol. 53 of interdisciplinary applied mathematics. New York: Springer
34. Schneider M, Josien M, Otto F (2022) Representative volume elements for matrix-inclusion composites—a computational study on the effects of an improper treatment of particles intersecting the boundary and the benefits of periodizing the ensemble. J Mech Phys Solids 158:104652
35. Dirrenberger J, Forest S, Jeulin D (2014) Towards gigantic rve sizes for 3d stochastic fibrous networks. Int J Solids Struct 51(2):359–376
36. Jeulin D (2016) Power laws variance scaling of boolean random varieties. Methodol Comput Appl Probab 18(4):1065–1079
37. Gloria A, Neukamm S, Otto F (2015) Quantification of ergodicity in stochastic homogenization: optimal bounds via spectral gap on glauber dynamics. Invent Math 199(2):455–515
38. Fischer J, Otto F (2017) Sublinear growth of the corrector in stochastic homogenization: optimal stochastic estimates for slowly

decaying correlations. Stoch Partial Differ Equ Anal Comput 5:220–255
39. Gloria A, Neukamm S, Otto F (2021) Quantitative estimates in stochastic homogenization for correlated coefficient fields. Anal PDE 14(8):2497–2537
40. Sab K, Nedjar B (2005) Periodization of random media and representative volume element size for linear composites. Comptes Rendus Mécanique 333(2):187–195
41. Elliott JC, Dover SD (1982) X-ray microtomography. J Microsc 126(2):211–213
42. Dame Carroll JR, Chandra A, Jones AS, Berend N, Magnussen JS, King GG (2006) Airway dimensions measured from micro-computed tomography and high-resolution computed tomography. Eur Respir J 28(4):712–720
43. Clozeau N, Josien M, Otto F, Xu Q (2024) Bias in the representative volume element method: periodize the ensemble instead of its realizations. Found Comput Math 24:1305–1387
44. Khoromskaia V, Khoromskij BN, Otto F (2020) Numerical study in stochastic homogenization for elliptic partial differential equations: convergence rate in the size of representative volume elements. Numer Linear Algebra Appl 27:e2296
45. Khoromskaia V, Khoromskij, BN (2020) Tensor-based techniques for fast discretization and solution of 3D elliptic equations with random coefficients, 1–25. arXiv:2007.06524
46. Schneider M (2021) A review of non-linear fft-based computational homogenization methods. Acta Mech 232:2051–2100
47. Moulinec H, Suquet P (1994) a fast numerical method for computing the linear and nonlinear mechanical properties of composites, comptes rendus de l'académie des sciences. Série II 318(11):1417–1423
48. Moulinec H, Suquet P (1998) A numerical method for computing the overall response of nonlinear composites with complex microstructure. Comput Methods Appl Mech Eng 157:69–94
49. Ye C, Chung ET (2023) Convergence of trigonometric and finite-difference discretization schemes for fft-based computational micromechanics. BIT Numer Math 63:11
50. Schneider M (2023) On the effectiveness of the Moulinec-Suquet discretization for composite materials. Int J Numer Meth Eng 124(14):3191–3218
51. Schneider M, Wicht D (2023) Superconvergence of the effective Cauchy stress in computational homogenization of inelastic materials. Int J Numer Meth Eng 124(4):959–978
52. Altendorf H, Jeulin D, Willot F (2014) Influence of the fiber geometry on the macroscopic elastic and thermal properties. Int J Solids Struct 51:3807–3822
53. Lubachevsky BD, Stillinger FH (1990) Geometric properties of random disk packings. J Stat Phys 60(5–6):561–583
54. Torquato S, Jiao Y (2010) Robust algorithm to generate a diverse class of dense disordered and ordered sphere packings via linear programming. Phys Rev E 82(6):061302
55. Bezrukov A, Bargie M, Stoyan D (2002) Statistical analysis of simulated random packings of spheres. Particle Particle Syst Charact 19:111–118
56. Josien M, Prat R (2024) Parallel and bias-free rsa algorithm for maximal Poisson-sphere sampling. Comput Phys Commun 305:109354
57. Williams S, Philipse A (2003) Random packings of spheres and spherocylinders simulated by mechanical contraction. Phys Rev E 67(5):1–9
58. Schneider M (2017) The sequential addition and migration method to generate representative volume elements for the homogenization of short fiber reinforced plastics. Comput Mech 59:247–263
59. Mattson W, Rice BM (1999) Near-neighbor calculations using a modified cell-linked list method. Comput Phys Commun 119:135–148
60. Advani SG, Tucker CL (1987) The use of tensors to describe and predict fiber orientation in short fiber composites. J Rheol 31(8):751–784
61. Kanatani K (1984) Distribution of directional data and fabric tensors. Int J Eng Sci 22:149–164
62. Köbler J, Schneider M, Ospald F, Andrä H, Müller R (2018) Fiber orientation interpolation for the multiscale analysis of short fiber reinforced composite parts. Comput Mech 61(6):729–750
63. Schneider M (2022) An algorithm for generating microstructures of fiber-reinforced composites with long fibers. Int J Numer Meth Eng 123(24):6197–6219
64. Lauff C, Schneider M, Montesano J, Böhlke T (2024) Generating microstructures of long fiber reinforced composites by the fused sequential addition and migration method. Int J Numer Meth Eng 125(22):e7573
65. Lauff C, Schneider M, Böhlke T (2025) Microstructure generation of long fiber reinforced hybrid composites using the fused sequential addition and migration method, J Thermoplast Compos Mater, vol. Online First
66. Bauer JK, Schneider M, Böhlke T (2023) On the phase space of fourth-order fiber-orientation tensors. J Elast 153:161–184
67. Verlet L (1967) Computer experiments on classical fluids. i. thermodynamical properties of Lennard-Ionear molecules. Phys Rev 159:98–103
68. Torquato S (2002) Random heterogeneous materials—microstructure and macroscopic properties. Springer, New York
69. Vondřejc J, Zeman J, Marek I (2014) An fft-based Galerkin method for homogenization of periodic media. Comput Math Appl 68(3):156–173
70. Willot F (2015) Fourier-based schemes for computing the mechanical response of composites with accurate local fields. Comptes Rendus Mécanique 343:232–245
71. Schneider M, Ospald F, Kabel M (2016) Computational homogenization of elasticity on a staggered grid. Int J Numer Meth Eng 105(9):693–720
72. Finel A (2025) A tetrahedron-based discretization for fft-based computational homogenization with smooth solution fields. Comput Methods Appl Mech Eng 436:117703
73. Schneider M, Merkert D, Kabel M (2017) Fft-based homogenization for microstructures discretized by linear hexahedral elements. Int J Numer Meth Eng 109(10):1461–1489
74. Leuschner M, Fritzen F (2018) Fourier-accelerated nodal solvers (fans) for homogenization problems. Comput Mech 62:359–392
75. Ladecký M, Leute RJ, Falsafi A, Pultarová I, Pastewka L, Junge T, Zeman J (2023) An optimal preconditioned fft-accelerated finite element solver for homogenization. Appl Math Comput 446:127835
76. Schneider M (2022) Voxel-based finite elements with hourglass control in fast Fourier transform-based computational homogenization. Int J Numer Meth Eng 123(24):6286–6313
77. Zeman J, Vondřejc J, Novák J, Marek I (2010) Accelerating a fft-based solver for numerical homogenization of periodic media by conjugate gradients. J Comput Phys 229(21):8065–8071
78. Brisard S, Dormieux L (2010) Fft-based methods for the mechanics of composites: a general variational framework. Comput Mater Sci 49(3):663–671
79. Lebensohn RA, Rollett AD (2020) Spectral methods for full-field micromechanical modelling of polycrystalline material. Comput Mater Sci 173:109336
80. Segurado J, Lebensohn RA, LLorca J, (2018) Chapter one—computational comogenization of polycrystals. Adv Appl Mech 51:1–114
81. Schneider M (2020) Lippmann-Schwinger solvers for the computational homogenization of materials with pores. Int J Numer Meth Eng 121(22):5017–5041

82. Hessman PA, Welschinger F, Hornberger K, Böhlke T (2021) On mean field homogenization schemes for short fiber reinforced composites: unified formulation, application and benchmark. Int J Solids Struct 230–231:111141
83. Mehta A, Schneider M (2022) A sequential addition and migration method for generating microstructures of short fibers with prescribed length distribution. Comput Mech 70(4):829–851
84. Schneider M (2019) On the Barzilai-Borwein basic scheme in fft-based computational homogenization. Int J Numer Meth Eng 118(8):482–494
85. Schneider M, Wicht D, Böhlke T (2019) On polarization-based schemes for the fft-based computational homogenization of inelastic materials. Comput Mech 64(4):1073–1095
86. Sab K (1992) On the homogenization and the simulation of random materials. Eur J Mech A Solids 11:585–607
87. Gélébart L, Ouaki F (2015) Filtering material properties to improve fft-based methods for numerical homogenization. J Comput Phys 294:90–95
88. Kabel M, Merkert D, Schneider M (2015) Use of composite voxels in fft-based homogenization. Comput Methods Appl Mech Eng 294:168–188
89. Lendvai J, Schneider M (2024) Assumed strain methods in micromechanics, laminate composite voxels and level sets. Int J Numer Meth Eng 125(11):e7459
90. Schneider K, Klusemann B, Bargmann S (2017) Fully periodic rves for technological relevant composites: not worth the effort! J Mech Mater Struct 12(4):471–484
91. Bris C, Legoll F, Minvielle M (2016) Special Quasirandom structures: a selection approach for stochastic homogenization. Monte Carlo Methods Appl 22(1):25–54
92. Fischer J (2019) The choice of representative volumes in the approximation of effective properties of random materials. Archive Ration Mech Anal 234(2):635–726

Publisher's Note Springer Nature remains neutral with regard to jurisdictional claims in published maps and institutional affiliations.